Available online at www.easd.procedia.org
EASD Procedia EURODYN (2026) 1277-1289

EASD Procedia

EURODYN 2026
XIII International Conference on Structural Dynamics
M. Beer, C. Papadimitriou, H. Jensen, J. Chen, M. Broggi, J. Behrensdorf (eds.)
Hannover, Germany, 27.09.–01.10 2026

IMAGE MEASUREMENT AND NUMERICAL SIMULATION OF RAIL DISPLACEMENT DISTRIBUTION DURING TRAIN PASSAGE AT A BRIDGE TRANSITION ZONE

Kodai Matsuoka[1] **and Koji Hattori**[2]

[1] Railway Technical Research Institute, Information and Communication Technology Division
2-8-38, Hikari-cho, Kokubunji-shi, Tokyo, 185-8540, Japan
e-mail: matsuoka.kodai.13@rtri.or.jp

[2] Railway Technical Research Institute, Railway Dynamics Division
2-8-38, Hikari-cho, Kokubunji-shi, Tokyo, 185-8540, Japan
hattori.koji.93@rtri.or.jp

Keywords: Rail displacement, Bridge transition zone, Lift-off, Nonlinear spring model.

Abstract. *This study quantitatively evaluates rail behavior and support conditions during train passage at structural boundaries consisting of a bridge, abutment, and embankment. A nonlinear finite element method that can account for variability in rail support stiffness, including lift-off, is developed. In the model, the rail and bridge are represented by beam elements, while the support system is modeled using nonlinear spring elements. Trilinear springs are introduced within the image measurement range to capture lift-off behavior, and a non-iterative solution method for stiffness equations involving multiple nonlinear springs is applied. Measured rail vertical displacement distributions obtained from image-based measurements using three video cameras are used for validation. Model parameters are calibrated to reproduce these measurements. The calculated rail displacement waveforms and distributions show good agreement with the measurements, confirming the validity of the proposed method. Further, the results indicate continuous lift-off of ~1–3 mm around the abutment on both the bridge and embankment sides, demonstrating that the proposed approach enables quantitative evaluation of spatial variability in support stiffness and its relationship with uplift behavior.*

ISSN:2311-9020 © 2026 The Authors. Published by EASD Procedia.
Peer-review under responsibility of the Organizing Committee of EURODYN 2026.
doi: 10.47964/1326.10740.243

1 INTRODUCTION

At structural boundaries where a bridge, an abutment, and an embankment is connected, rail support stiffness varies significantly across locations. In particular, increased rail settlement in the ballast section behind the abutment, hanging sleepers due to ballast degradation beneath rail-supporting sleepers, and rail uplift are well-known weak points from a track maintenance perspective [1].

To mitigate rail settlement, countermeasures such as gradual transitions in rail support stiffness in the boundary region have been investigated. For newly constructed embankments, design standards specify the installation of relatively high-stiffness approach blocks behind the abutment. In addition, for existing embankments, experimental and numerical studies have examined measures such as subgrade improvement [1].

Furthermore, at locations where hanging sleepers occur, repeated impacts between ballast and sleepers during train passage accelerate track deterioration. Although hanging sleepers cannot be observed under unloaded conditions, they exhibit significantly greater settlement during train passage than sound sleepers [2]. Consequently, they may adversely affect ride comfort and running safety, and studies have explored detection methods using onboard measurements for track management [3,4].

However, at structural boundaries, variability in rail support conditions, including the presence of hanging sleepers, produces complex and location-dependent rail displacement behavior during train passage [5]. In recent years, studies have also examined the dynamic behavior of bridges, abutments, and embankments under train loading [6]. From a field measurement perspective, wide-area rail displacement distributions across bridges, abutments, and embankments have been visualized using image-based techniques with three video cameras and subsequent image synthesis [7]. Meanwhile, in examining countermeasures against settlement, such as determining the type and extent of interventions, rail support conditions must be quantitatively evaluated—such as support stiffness, uplift magnitude, and the distribution of hanging sleepers—particularly in the embankment behind the abutment at structural boundaries [8]. However, methodologies for quantitatively evaluating these conditions across bridge, abutment, and embankment sections based on rail displacement distributions remain insufficiently established.

Given the above context, this study develops a numerical analysis method that accounts for variability in rail support conditions, including hanging sleepers, at structural boundaries composed of bridges, abutments, and embankments. Furthermore, by comparing rail displacement distributions calculated using the proposed method (after parameter calibration) with those obtained from image-based measurements, the validity of the proposed method and the behavior at the target site are examined.

2 NUMERICAL ANALYSIS METHOD CONSIDERING VARIABILITY IN SUPPORT CONDITIONS INCLUDING LIFT-OFF

2.1 Existing analysis methods

Several numerical approaches have been proposed to evaluate rail displacement behavior during train passage. For example, some methods iteratively correct rail deflection by enforcing equilibrium between external and reaction forces based on the positional relationship between rail deflection and a prescribed lift-off amount, thereby estimating rail settlement [9]. In addition, two-dimensional (2D) nonlinear static analyses using general-purpose analysis software have been employed. Furthermore, a method has been proposed in which bearing looseness in bridge girders—where gaps occur at supports and induce uplift-like motion during

train passage—is modeled using a bilinear nonlinear spring with a single breakpoint, and the associated stiffness equations (including this nonlinear spring) are solved without iterative convergence calculations [10].

In this study, to enable comparison between analytical results and measurements, a site similar to that examined in previous studies [7,10]—where rail displacement distributions across bridge, abutment, and embankment sections were measured—was selected. At the target site, field measurements using gap gauges confirmed the presence of gaps between some sleepers on the bridge and the upper flange. In addition, rail displacement distributions obtained from image-based measurements suggest the presence of hanging sleepers in part of the embankment section behind the abutment [10]. Therefore, to reproduce the measured rail displacement distributions, nonlinear springs with three types of rail support stiffness at multiple locations must be assigned: (i) when vertical rail settlement directly above a sleeper is smaller than the lift-off amount, (ii) when it exceeds the lift-off amount, and (iii) when upward vertical displacement occurs.

In this study, to reduce computational cost in future applications such as inverse analysis, a trilinear nonlinear spring (three-stage linear spring) with two breakpoints—at zero rail vertical displacement and at the lift-off amount—is introduced for each of the 20 fastenings within the image measurement range. Furthermore, an analysis method is proposed that enables the introduction of such nonlinear springs at multiple locations—unlike conventional approaches that apply them only at a single location for modeling bearing looseness—and that does not require iterative calculations.

2.2 Numerical model

Figure 1 shows the beam–spring model of the structural boundary analyzed in this study. The rail and the bridge were modeled using Euler–Bernoulli beam elements, while the rail support system—comprising rail fastening components (rail pads, sleepers, ballast, and subgrade) and bridge bearings—was modeled using vertical spring elements. A series of moving loads positioned on the modeled rail was incrementally shifted, and static analyses were conducted at each step. Although wheel loads on left and right rails may differ during train passage, their mutual influence is relatively small [11]. Therefore, only one rail—the right rail when facing the origin side (i.e., the side captured by the video cameras in the field measurements)—was considered in the model.

To enable comparison with rail displacement waveforms and distributions obtained from image-based measurements, model parameters were defined on the basis of field measurement conditions reported in a previous study [10]. The target site is located near the end of a conventional railway bridge crossing a river, consisting of five simply supported steel deck girders (each with a bridge length of 13.4 m and a span length of 12.9 m) [10]. However, this study focused on the structural boundary where field measurements were conducted. Therefore, only the simply supported girder connected to the abutment (one span of a steel deck girder) was considered.

In addition to the 20 fastenings for which rail vertical displacement during train passage was obtained, prerunning and postrunning sections were introduced to minimize boundary effects on sleepers corresponding to indices −6 and 13 (see Figure 2). Specifically, an additional 5 m (equivalent to eight fastenings) was added on the terminal side beyond sleeper No. 13, and another 5 m (eight fastenings) was added on the origin side from the bridge end. The conditions of the image measurements used for comparison are described in detail in Section 3.1.

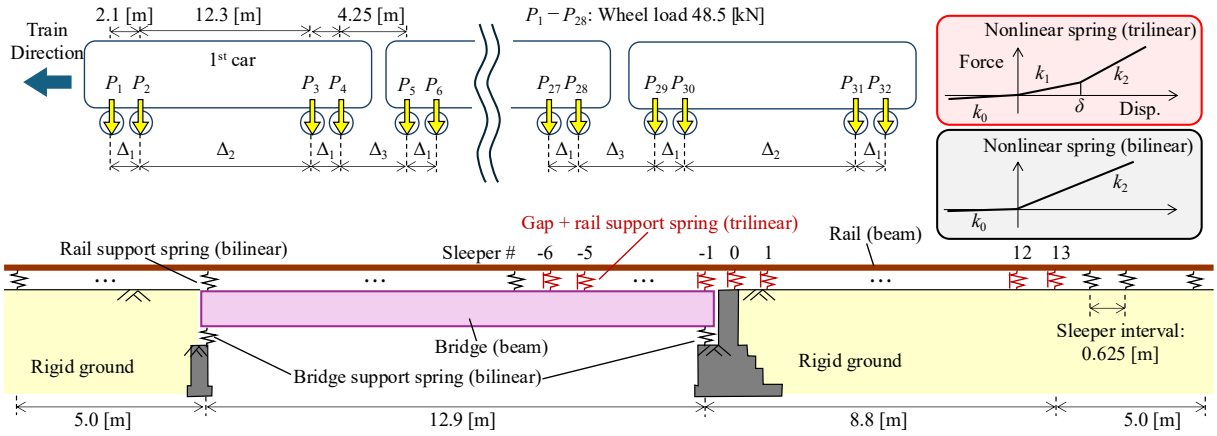


Figure 1: 2D nonlinear finite element method (FEM) model of a structural boundary accounting for variability in rail support conditions, including lift-off.

Figure 1 also illustrates the load train corresponding to an eight-car train set passing during the field measurements. The train traveled at ~81 km/h (22.5 m/s). Because the video cameras operated at 60 fps, the train advanced 0.375 m per frame. In the finite element method (FEM) analysis, to achieve a resolution finer than the image measurement frame rate, the load train was incrementally moved by 0.300 m per step from right to left (i.e., from the terminal side to the origin side), as shown in Figure 1.

However, because axle positions generally do not coincide with rail node locations, rail discretization can introduce approximation errors. In this study, following Hattori et al. [11], the rail was discretized into four elements per fastening interval. When an axle was located within a beam element (i.e., between nodes), the load was distributed to adjacent nodes in proportion to their distances from the axle position.

2.3 Nonlinear springs

As the 20 fastenings analyzed in the image measurements may include hanging sleepers, trilinear nonlinear springs (three-stage linear springs) were adopted as support springs to reproduce the behavior associated with such conditions. For rail support regions outside the analysis range, lift-off was not assumed. In addition, no bearing lift-off was observed at bridge supports in the field measurements [7]. Therefore, these locations were modeled using bilinear nonlinear springs (two-stage linear springs).

The trilinear springs represented rail behavior over hanging sleepers by assigning the following support stiffness values:

- Zero-order stiffness k_0: support stiffness when the rail support system acted in tension under upward vertical rail displacement.
- Primary stiffness k_1: very small stiffness when downward rail displacement is smaller than the lift-off amount.
- Secondary stiffness k_2: support stiffness when the rail support system acts in compression after downward rail displacement exceeds the lift-off amount.

For bilinear springs, because lift-off was not considered, only zero-order and secondary stiffness components were defined (i.e., no distinction between primary and secondary stiffness in the compressive regime). The secondary stiffness was set to be sufficiently larger than the zero-order and primary stiffness values under lift-off conditions ($k_0, k_1 \ll k_2$). The specific stiffness values at each stage are detailed in Section 3.2.

Notably, whereas some modeling approaches assign separate stiffness values to individual components (e.g., rail pads and vibration isolation pads) and connect them in series [11], this

study adopted an equivalent composite support stiffness representing all rail-supporting elements to facilitate the evaluation of variability in rail support conditions.

Trilinear springs were introduced at rail fastening positions over the embankment behind the abutment on the train-entry side (sleepers 13 to 1), at the abutment (sleeper 0), and on the bridge (sleepers −1 to −6). The rail node coordinates were adjusted to match the measured sleeper spacing obtained from image measurements. Outside the measurement range, bilinear springs were applied, and the sleeper spacing was set to 0.625 m following typical fastening intervals [12], corresponding to an element length of 0.156 m when divided into four elements per interval.

2.4 Solution method for the stiffness equation

In general, stiffness equations that include multiple nonlinear springs are solved using iterative convergence methods. However, in this study, to facilitate future extension to inverse analysis, a noniterative solution method is adopted, as outlined below.

The method proposed by Hattori et al. [12] for a system with a single nonlinear spring is extended here to cases involving multiple nonlinear springs. In the following, trilinear and bilinear springs are treated uniformly as nonlinear springs. This is because a bilinear spring can be regarded as a special case of a trilinear spring where the lift-off amount is arbitrarily defined and the primary and secondary stiffness values are equal ($k_1 = k_2$). However, because variables involving the lift-off amount appear in the denominator, a positive value must be assigned to the lift-off amount in practice, even for bilinear springs. Notably, only vertical loads and displacements are considered in this study, and rotational effects are neglected.

First, a stiffness matrix K_1 is constructed by considering only k_1 of the nonlinear springs. From this matrix, a provisional displacement vector x^* for all nodes under the external force vector F is obtained from the stiffness equation:

$$x^* = K_1^{-1}F \tag{1}$$

From the relative displacements between the two nodes of each nonlinear spring at position s $(s = 1, \dots, S)$, a provisional spring displacement δ_s^* is obtained. This represents the displacement that would occur if the nonlinear spring behaved linearly with $k_{1(s)}$. Let δ_s denote the breakpoint displacement between the primary and secondary stiffness regions (i.e., the lift-off amount at position s). Then, defining the ratio $r_s = \delta_s^*/\delta_s$, the ratio vector r for all spring locations is expressed as

$$r = [r_1, \dots, r_S] = \left[\frac{\delta_1^*}{\delta_1}, \dots, \frac{\delta_S^*}{\delta_S}\right] \tag{2}$$

Here, for a nonlinear spring at position s:

- when $r_s \geq 1$, the spring reaches the secondary stiffness region;
- when $0 \leq r_s < 1$, it remains within the primary stiffness region;
- when $r_s < 0$, it is in the zero-stiffness region (i.e., upward rail displacement occurs).

Let P_s denote the load acting on the nonlinear spring at position s due to the external force vector F. By multiplying P_s by the reciprocal of each component of the ratio vector r (i.e., $(r_1, \dots, r_S)^{-1}$), the resulting values are arranged in ascending order, as shown in Eq. (3):

$$\frac{P_s}{r_a} < \frac{P_s}{r_b} < \cdots (< 0) < \cdots < \frac{P_s}{r_c} < \frac{P_s}{r_s} < \frac{P_s}{r_d} < \cdots < \frac{P_s}{r_e} < \frac{P_s}{r_f} \tag{3}$$

where $a, b, c, d, e,$ and f denote different nonlinear spring locations. In the following, the solution procedure is described by classifying cases in accordance with the ordering in Eq. (3) and the conditions derived from the ratio vector r.

Condition I: When the nonlinear spring at location s reaches the secondary stiffness region($1 \le r_s \Rightarrow P_s/r_s \le P_s$), it is defined as follows. As shown in Figure 2(a), $k_{1(s)}$ is applied up to the breakpoint between the primary and secondary stiffness regions, and $k_{2(s)}$ is applied thereafter. Accordingly, the relative displacement δ_s' between the two nodes of the nonlinear spring at location s can be calculated using Eq. (4):

$$\delta_s' = \frac{P_s/r_s}{k_{1(s)}} + \frac{P_s - P_s/r_s}{k_{2(s)}} = \frac{P_s/r_a}{k_{1(s)}} + \frac{P_s/r_b - P_s/r_a}{k_{1(s)}} + \cdots + \frac{P_s/r_f - P_s/r_e}{k_{2(s)}} + \frac{P_s - P_s/r_f}{k_{2(s)}} \quad (4)$$

This expression represents the displacement as the cumulative contribution of segments partitioned according to stiffness transition points defined by the ratio vector.

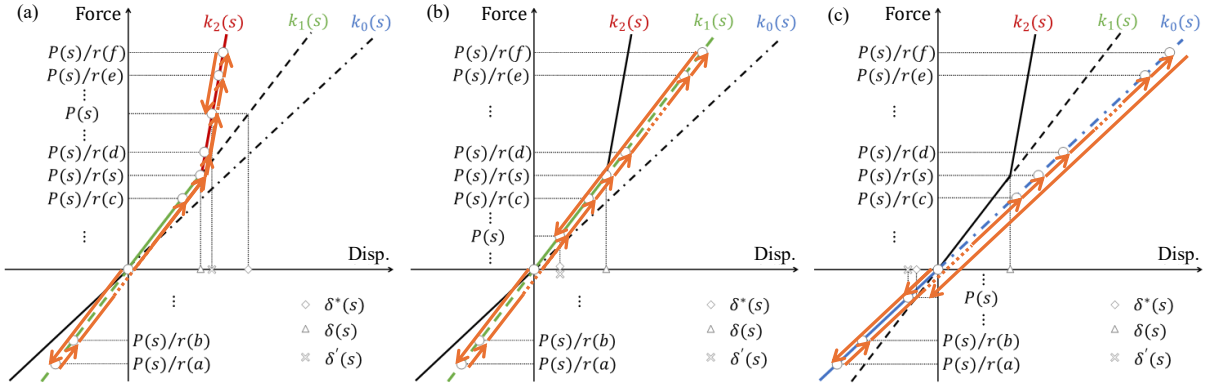


Figure 2: Conceptual force–displacement relationships of nonlinear springs at location s: (a) secondary stiffness region (Condition I), (b) primary stiffness region (Condition II), and (c) zero-stiffness region (Condition III).

Condition II: When the nonlinear spring at location s remains in the primary stiffness region ($0 \le r_s < 1 \Rightarrow 0 \le P_s < P_s/r_s$), it is defined as follows. As shown in Figure 2(b), only $k_{1(s)}$ is applied. Accordingly, the relative displacement δ_s' between the two nodes of the nonlinear spring at location s can be calculated using Eq. (5):

$$\delta_s' = \frac{P_s/r_s}{k_{1(s)}} + \frac{P_s - P_s/r_s}{k_{1(s)}} = \frac{P_s/r_a}{k_{1(s)}} + \frac{P_s/r_b - P_s/r_a}{k_{1(s)}} + \cdots + \frac{P_s/r_f - P_s/r_e}{k_{2(s)}} + \frac{P_s - P_s/r_f}{k_{2(s)}} \quad (5)$$

Because the spring response remains entirely within the primary stiffness region, the displacement is expressed solely using $k_{1(s)}$ over the entire load range.

Condition III: When the nonlinear spring at location s is in the zero-stiffness region and upward rail displacement occurs ($r_s < 0 \Rightarrow P_s < 0$), it is defined as follows. As shown in Figure 2(c), only $k_{0(s)}$ is applied. Accordingly, the relative displacement δ_s' between the two nodes of the nonlinear spring at location s can be calculated using Eq. (6):

$$\delta_s' = \frac{P_s/r_s}{k_{0(s)}} + \frac{P_s - P_s/r_s}{k_{0(s)}} = \frac{P_s/r_a}{k_{0(s)}} + \frac{P_s/r_b - P_s/r_a}{k_{0(s)}} + \cdots + \frac{P_s/r_f - P_s/r_e}{k_{0(s)}} + \frac{P_s - P_s/r_f}{k_{0(s)}} \quad (6)$$

Equations (4)–(6) represent the accumulation of displacements from the origin, consistent with the orange arrows shown in Figures 2(a)–(c). Although the types of stiffness used in the calculation differ depending on Conditions I–III, the mathematical form of these equations is

identical. Therefore, under the ordering relation defined in Eq. (3), the displacement vector for all nodes x' can be expressed as follows:

$$x' = \grave{K}^{-1}_{[0\to A]}\frac{F}{r_a} + \grave{K}^{-1}_{[A\to B]}\left(\frac{F}{r_b}-\frac{F}{r_a}\right) + \cdots + \grave{K}^{-1}_{[F\to P]}\left(F-\frac{F}{r_f}\right) \tag{7}$$

Here, $\grave{K}$ denotes the stiffness matrix whose components are determined by the state of each nonlinear spring (i.e., whether it is in the primary, secondary, or zero-stiffness region). The subscripts of $\grave{K}$ indicate load increments corresponding to each displacement segment. For example, $[\,0 \to A\,]$ represents the case where the load at each nonlinear spring location changes from 0 to P_s/r_a. Similarly, $[\,A \to B\,]$ corresponds to the transition from P_s/r_a to P_s/r_b, and the final term $[\,F \to P\,]$ represents the adjustment from P_s/r_f to the target load P_s.

Thus, Eq. (7) consists of $S + 1$ terms: S terms corresponding to the nonlinear springs in the model, each having different lift-off values, and one additional term that corrects the displacement from P_s/r_f to P_s.

3 REPRODUCTION RESULTS

3.1 Image measurement results

The measured data used in this study were obtained through image-based measurement. Detailed information on the field measurements is provided in Yotsui et al. [7], while an overview is presented below.

Figure 3 shows an overview of the structural boundary analyzed in this study. As described in Section 2.2, the site is located near the terminal side of a conventional railway bridge crossing a river and consists of bridge, abutment, and embankment sections. The measurement range covered 20 fastenings: six on the bridge (terminal side), one on the abutment, and 13 on the embankment behind the abutment. Rail vertical displacement during train passage was measured for one rail—the right rail when facing the origin side (the near side in Figure 3)—using three video cameras.



Figure 3: Overview of the measured structural boundary.

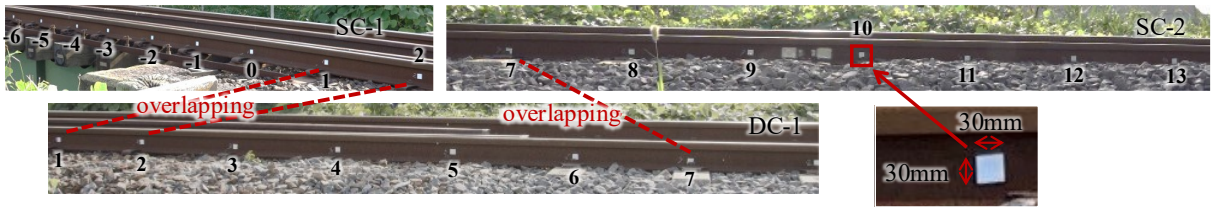


Figure 4: Measurement setup for rail vertical displacement using three video cameras and rail markers.

Figure 4 shows the camera configurations and marker placement for the three video cameras. In the field measurements, rail behavior must be captured over a wide range spanning the bridge, abutment, and embankment through simultaneous multipoint measurement. Thus, an image-based measurement technique was adopted. However, because of limitations in camera field of view, using a single camera would require either a wide-angle setting or distant placement, which reduces resolution and, consequently, measurement accuracy.

To address this issue, three video cameras (camera IDs: SC-1, DC-1, and SC-2) were positioned with partially overlapping fields of view. The rail displacement obtained from each camera was then synchronized in time and combined to generate a continuous wide-area displacement distribution. All cameras were installed on stable ground ~3–4 m away from the track on the embankment behind the abutment using tripods. The frame rate for all three cameras was 60 fps.

To ensure sufficient image processing accuracy for the rail regions near the edges of the field of view, where the rail was captured obliquely, white magnetic sheets (Figure 4) were installed as markers on the rail web directly above each sleeper. In the image processing procedure, rail vertical displacement was measured by tracking these markers using the digital image correlation method [13], and pixel-based measurements were converted to physical dimensions using the marker size (30 mm × 30 mm).

To obtain rail vertical displacements above the sleepers for the 20 fastenings, a sparse search based on template matching was first performed to estimate pixel-level displacements, followed by subpixel estimation to capture movements smaller than one pixel. Details of these procedures are provided in Matsuoka et al. [13]. When converting pixel measurements to physical dimensions, the spatial resolutions were ~1.5–2.6 mm/pixel for cameras SC-1 and SC-2 and 0.52–0.66 mm/pixel for camera DC-1.

3.2 Parameter estimation

As described in Section 2.3, trilinear nonlinear springs were assigned to represent rail support stiffness for the 20 fastenings within the image measurement range, where hanging sleepers were suspected, whereas bilinear nonlinear springs were used at other locations and for bridge bearings. To evaluate rail behavior at the measurement site, appropriate parameters must be input into the FEM model constructed in Section 2, and the resulting rail displacement waveforms and distributions must be compared with those obtained from image-based measurements. In this study, the FEM parameters were systematically calibrated to reproduce the measured data, as described below.

First, based on material test results [14], the rail support stiffness values at all locations—including the 20 fastenings—were initially set as follows: k_0, k_1, and $k_2$were all assigned a value of 4×10^7 N/m, and the lift-off amount δ was set to 0 mm. Subsequently, the parameters governing the rail support conditions within the 20 fastenings were determined in three steps, as outlined below.

Setting A: k_2 is adjusted so that the minimum displacement of the waveform calculated using FEM matches that of the waveform obtained from image measurements at each location. In this step, both k_1 and k_2 are set to 4×10^6 N/m.

Setting B: Because lift-off is not considered in Setting A, the estimated k_2 may become excessively small. Therefore, the lift-off amount δ and the primary stiffness k_1 are introduced. The primary stiffness k_1 is set to be significantly smaller than the secondary stiffness (specifically, $k_1 = k_2/10^2$). The validity of this assumption is discussed in Section 3.3. The lift-off amount δ is increased incrementally by 1 mm, and k_2 is adjusted accordingly until good agreement with the measured rail displacement waveform is achieved. A practical considera-

tion here—slightly subtle but important—is that the applied load is distributed among multiple neighboring support points. Consequently, modifying parameters at one location affects load sharing and displacement behavior at adjacent locations. Although the extent of this influence depends on the support conditions and sleeper spacing, it generally decreases with distance from the modified location. Hence, after adjusting the parameters at a given location s, fine-tuning should be performed sequentially for neighboring locations ($s-1$, $s+1$, and so on).

Setting C: k_0 is determined so that the upward displacement due to uplift—occurring with the abutment acting as a pivot—is also reproduced.

The rail support stiffness and lift-off amounts obtained from Settings A to C for the 20 fastenings are summarized in Table 1. Meanwhile. Table 2 presents the parameters for the rail, the support system outside the measurement range, the bridge, and the bridge bearings.

Notably, this study does not aim to perform inverse analysis but rather to quantitatively evaluate support conditions based on measured rail displacements. In addition, considering the accuracy of image measurement and processing, the support stiffness and lift-off values are treated with one significant digit.

Section	Bridge						Abut.	Embankment	
Sleeper #	−6	−5	−4	−3	−2	−1	0	1	2
$k_{0(s)}$ [N/m]	5×10^5	4×10^6	4×10^6	4×10^5	4×10^4	4×10^4	4×10^7	4×10^6	4×10^6
$k_{1(s)}$ [N/m]	5×10^5	9×10^6	1×10^5	8×10^4	8×10^4	9×10^4	4×10^7	5×10^6	4×10^4
$k_{2(s)}$ [N/m]	4×10^8		1×10^7	8×10^6	8×10^6	9×10^6			4×10^6
$\delta_{(s)}$ [mm]	1	—	2	2	3	2	—	—	2

Embankment										
3	4	5	6	7	8	9	10	11	12	13
4×10^4	4×10^4	4×10^4	4×10^4	4×10^4	4×10^4	4×10^4	4×10^4	4×10^7	1×10^7	3×10^6
7×10^6	7×10^4 7×10^6	7×10^4 7×10^6	7×10^4 7×10^6	7×10^4 7×10^6	1×10^7	3×10^7	4×10^7	4×10^7	1×10^7	3×10^6
—	2	2	1	3	—	—	—	—	—	—

Table 1: Support stiffness assigned to the nonlinear spring (within the image measurement range).

Elements	Beam	
	Rail	Bridge
EI [N · m^2]	6.47×10^6	1.41×10^9
m [kg/m]	60.8	231.5
Elements	Spring	
	Rail supports (Outside the measurement range)	Bridge supports
$k_{0(s)}$ [N/m]	4×10^7	1×10^{11}
$k_{1(s)}$ [N/m]		
$k_{2(s)}$ [N/m]		
$\delta_{(s)}$ [mm]	—	—

Table 2: Parameters assigned to the bridge and rail.

3.3 Application results

The parameters shown in Tables 1 and 2 were applied to the FEM model constructed in Section 2. Figure 5 presents the rail displacement waveforms for the 20 fastenings within the

image measurement range (sleepers −6 to 13). Figure 6 shows the rail displacement distributions under two conditions: (a) when the moving load is located in the embankment behind the abutment and uplift-induced upward displacement occurs at the bridge end and (b) when the moving load is located at the bridge end and uplift-induced upward displacement occurs in the embankment behind the abutment. In these figures, gray solid lines represent rail vertical displacements obtained from image-based measurements, orange solid lines indicate those calculated using the FEM model, and blue arrows denote the positions of the moving load.

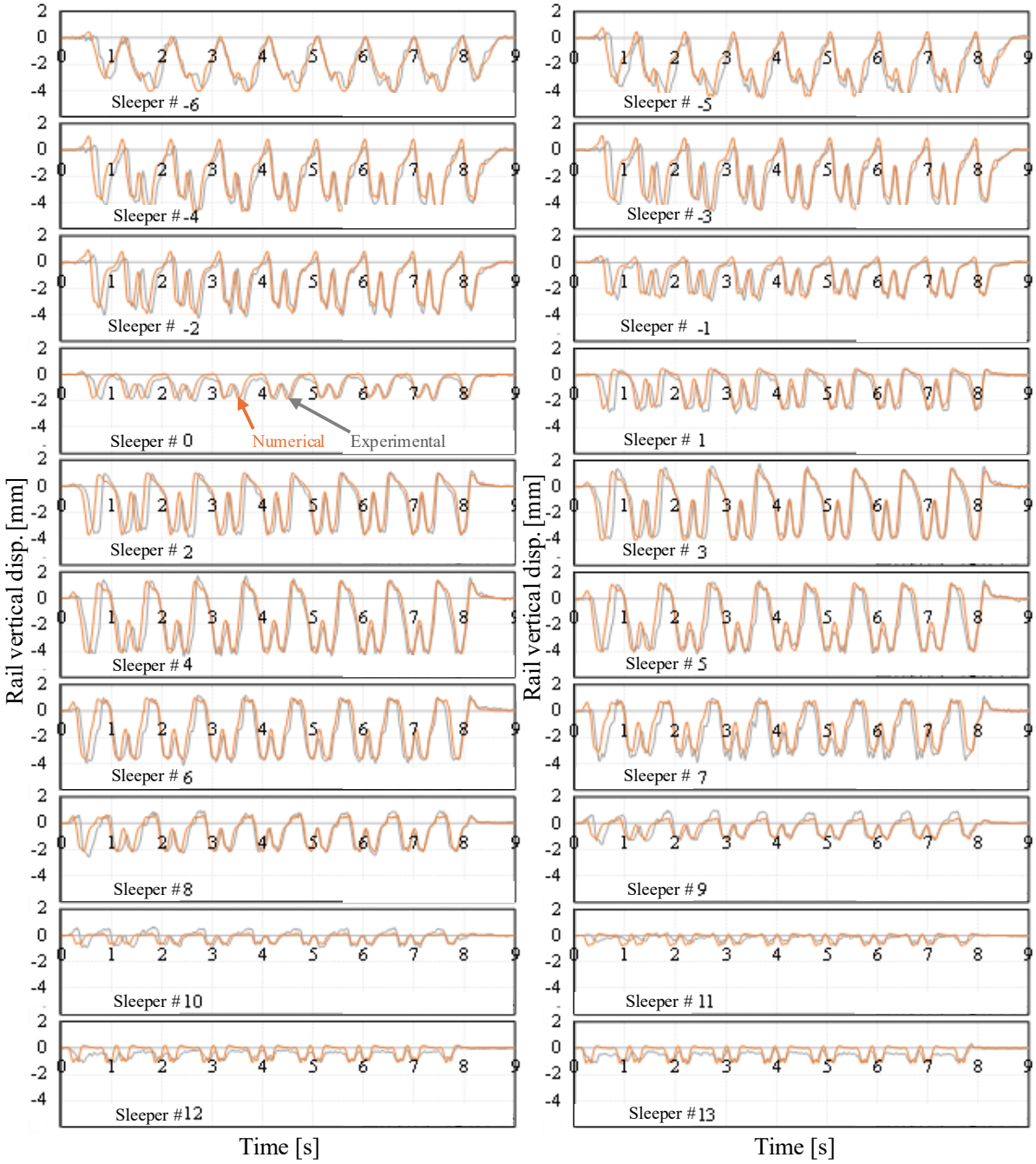


Figure 5: Rail displacement waveforms for 20 fastenings across the structural boundary.

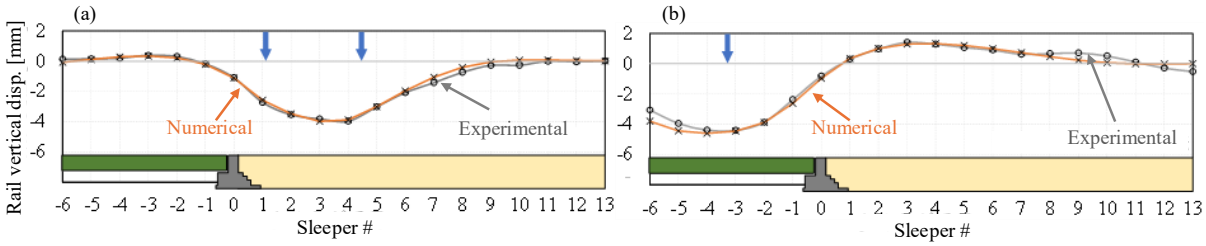


Figure 6: Rail displacement distribution at the structural boundary: (a) bridge-end uplift; (b) backfill uplift behind the abutment.

Because the rail displacement waveforms and distributions at each location show good agreement, it can be concluded that the constructed model and solution method can accurately reproduce complex rail behaviors at the structural boundary during train passage, including uplift about the abutment as a pivot. Therefore, the parameters listed in Tables 1 and 2 are considered to be generally appropriate. As shown in Table 1, the estimated rail support stiffness varies significantly across locations, and lift-off of ~1–3 mm is identified over four fastenings on the bridge side and seven on the embankment side from the abutment. Please note that the rail support structures differ between bridges and embankments, and therefore the meaning of the support stiffness differs as well: on bridges, it refers to the bridge sleepers and rail pads, while on embankments, it refers to the ballast, sleepers, and rail pads. In addition, a previous study [1] reported that at locations with hanging sleepers, repeated impacts between ballast and sleepers during train passage can cause ballast degradation, leading to reduced support stiffness. This observation is consistent with the present results.

In the embankment behind the abutment, starting from around sleeper 9, no lift-off was observed and a relatively large number of sleepers maintained sufficient support capacity. Therefore, when an axle was located in this embankment section, sleepers with higher support stiffness—specifically sleeper 0 on the abutment and sleeper 9 on the embankment—acted as supports. Consequently, a deformation shape resembling a half-sine wave was generated between sleepers 1 and 8, leading to rail uplift near the bridge end. Similarly, sleeper 0 on the abutment and a location around sleeper −5 on the bridge acted as supports, resulting in larger settlement in the region of sleepers −1 to −4, near the bridge end, compared with sleeper −6 near midspan. This behavior was considered to contribute to uplift in the embankment section behind the abutment. Given these considerations, it is inferred that locations with significantly reduced rail support due to lift-off are not isolated but occur continuously across the structural boundary. This continuity leads to larger settlements and, through stiffer regions such as the abutment, induces uplift on the opposite side of the rail. Although previous research [3] has identified differences in rail support stiffness as a primary cause of uplift-induced upward displacement, this study demonstrated that the magnitude and spatial extent of lift-off and rail support stiffness can be quantitatively evaluated through waveform reproduction analysis.

Meanwhile, because the image measurement range in this study was limited to sleepers −6 to 13, the rail support parameters could be individually calibrated only for these 20 fastenings. As shown in Table 2, sleepers outside this range were uniformly assigned a stiffness of 4×10^7 N/m. Consequently, at boundary locations, such as sleepers −6 and 13, the surrounding support conditions may not be accurately represented, resulting in the lower reproducibility of the displacement waveforms. Indeed, as shown in Figure 5 for sleepers 12 and 13, the measured rail displacement did not fully return to zero between successive axle passages. This suggests that regions with lower support stiffness than those assumed in this study may exist beyond sleeper 14. For future applications of the proposed model to other structural boundaries, acquiring measurement data not only within the target region but also over several fas-

tenings before and after the region of interest is expected to improve the accuracy of waveform reproduction at boundary locations.

In addition, Figure 6 shows a slight discrepancy in the time axis of the calculated waveforms for the first to third bogies compared with the measured results. This could be attributed to a reduction in train speed during measurement due to a station located in the upstream direction of travel.

Looking ahead to inverse analysis, a similar approach to that adopted in this study—incrementally increasing the lift-off amount and adjusting the secondary stiffness to match measured waveforms—may enable efficient estimation despite the large number of parameters (20 fastenings × [three stiffness values + one lift-off parameter] = 80 parameters). Because the constructed model considered only quasistatic behavior, each time step was independent, allowing efficient parallel computation. In this study, parallel computation was performed using MATLAB's Parallel Computing Toolbox. The computation time was ~5.3 s using a 32-core (3.6 GHz) processor, indicating that the proposed model is sufficiently efficient for use as a fundamental model for inverse analysis.

4 CONCLUSIONS

In this study, a nonlinear FEM that can account for variability in rail support stiffness (including lift-off) was developed to quantitatively evaluate rail behavior and support conditions at structural boundaries where a bridge, abutment, and embankment are connected. The validity of the proposed method was examined by comparing calculated rail displacement distributions with those obtained from image-based measurements, and the rail support stiffness and lift-off amounts were quantitatively evaluated. Furthermore, parametric analyses were conducted using the developed FEM by varying the rail support stiffness and lift-off values to investigate rail behavior under various conditions. The main findings are summarized as follows:

- The rail displacement waveforms and distributions for the 20 fastenings calculated using the proposed FEM and the noniterative solution method for the stiffness equation showed good agreement with the image-based measurement results, confirming that the proposed method accurately reproduces complex rail behavior at structural boundaries during train passage.
- At the structural boundary considered in this study, lift-off of ~1–3 mm occurred continuously over four fastenings on the bridge side and seven on the embankment side from the abutment.

REFERENCES

[1] Katsumi Muramoto, Takahisa Nakamura, and Tasuku Sakura. "A Study of the Effect of Track Irregularity Prevention Methods for the Transition Zone Between Different Track Structures". In: *Quarterly Report of RTRI* 53.4 (2012), pp. 211–215. DOI: 10.2219/rtriqr.53.211.

[2] Haruki Yotsui, Kodai Matsuoka, Kiyoyuki Kaito and Koji Hattori. "Evaluation of Floating Sleepers on Bridges Using Full-Field Image Measurement". In: *Jpn J JSCE* 81.15 (2025), 24-15008. DOI: 10.2208/jscejj.24-15008. (In Japanese).

[3] Daiki Yamaoka, Masanobu Kusuda, Hirofumi Tanaka, Mami Matsumoto, and Hiroo Kataoka. "Proposal for Unsupported Sleeper Detection Method and Utilization in Track

Maintenance". In: *Quarterly Report of RTRI* 63.1 (2022), pp. 25–30. DOI: 10.2219/rtriqr.63.1_25.

[4] Masaru Kitahara, Daichi Masuda, Kai Xue, Tomonori Nagayama, Di Su, and Hirofumi Tanaka. "Track Geometry Estimation and Hanging Sleeper Detection Using Vehicle Dynamic Responses with Unknown System Parameters". In: *ASCE-ASME Journal of Risk and Uncertainty in Engineering Systems, Part A: Civil Engineering* 10.3 (2024), 04024044. DOI: 10.1061/AJRUA6.RUENG-1259.

[5] André Paixão, Eduardo Fortunato, and Rui Calçada. "Transition Zones to Railway Bridges: Track Measurements and Numerical Modelling". In: *Engineering Structures* 80 (2014), pp. 435–443. DOI: 10.1016/j.engstruct.2014.09.024.

[6] A. Jain, A. V. Metrikine, M. J. M. M. Steenbergen and K. N. Van Dalen. "Railway Transition Zones: Evaluation of Existing Transition Structures and a Newly Proposed Transition Structure". In: *International Journal of Rail Transportation* 12.6 (2024), pp. 979–999. DOI: 10.1080/23248378.2023.2272668.

[7] Haruki Yotsui, Kodai Matsuoka, and Kiyoyuki Kaito. "Data Fusion Method for Displacement Distribution Measurement Using Multiple Cameras: Application to Rail Displacement". In: *International Conference on Experimental Vibration Analysis for Civil Engineering Structures*. Cham: Springer Nature Switzerland, 2025, pp. 566–575. DOI: 10.1007/978-3-031-96106-9_59.

[8] Mykola Sysyn, Olga Nabochenko, and Vitalii Kovalchuk. "Experimental Investigation of the Dynamic Behavior of Railway Track with Sleeper Voids". In: *Railway Engineering Science* 28.3 (2020), pp. 290–304. DOI: 10.1007/s40534-020-00217-8.

[9] Takahiro Suzuki, Makoto Ishida, Kazuhisa Abe, and Kazuhiro Koro. "Measurement on Dynamic Behaviour of Track Near Rail Joints and Prediction of Track Settlement". In: *Quarterly Report of RTRI* 46.2 (2005), pp. 124–129. DOI: 10.2219/rtriqr.46.124.

[10] Tadafumi Takase, Kodai Matsuoka, Kiyoyuki Kaito and Haruki Yotsui. "Numerical Study of Rail Support Condition Effect on the Rail Behavior Under Train Passage at Bridge–Abutment–Embankment Section". In: *Journal of Structural Engineering A* 71 (2025), pp. 12–25. DOI: 10.11532/structcivil.71A.12. (In Japanese).

[11] Koji Hattori, Kodai Matsuoka, and Hirofumi Tanaka. "Development of the Bridge Deflection-Track Irregularity Conversion Program for the Deflection Estimation Method Based on Track Irregularities". In: *Japanese Journal of JSCE* 80.15 (2024), 23-15047. DOI: 10.2208/jscejj.23-15047. (In Japanese).

[12] Koji Hattori, Kodai Matsuoka, and Hirofumi Tanaka. "Evaluation of the Effect of Loose Bridge Bearing on Onboard Measured Track Geometry Using Numerical Analysis". In: *Quarterly Report of RTRI* 66.4 (2025), pp. 262–268. DOI: 10.2219/rtriqr.66.4_262.

[13] Kodai Matsuoka, Fumiaki Uehan, Hiroya Kusaka, and Hikaru Tomonaga. "Experimental Validation of Non-Marker Simple Image Displacement Measurements for Railway Bridges". In: *Applied Sciences* 11.15 (2021), 7032. DOI: 10.3390/app11157032.

[14] Kodai Matsuoka, Kazuhiro Kajihara, and Hirofumi Tanaka. "Identification of Vibration Modes and Wave Propagation of Operational Rails by Multipoint Hammering and Reciprocity Theorem". In: *Materials* 15.3 (2022), 811. DOI: 10.3390/ma15030811.